Earth and Space Science

RESEARCH ARTICLE
10.1029/2022EA002513

Aurora Detection From Nighttime Lights for Earth and Space Science Applications

Virginia Kalb[1], Burcu Kosar[1,2], Yaireska Collado-Vega[1], and Carol Davidson[1,3]

[1]NASA Goddard Space Flight Center, Greenbelt, MD, USA, [2]The Catholic University of America, Washington, DC, USA, [3]Science Systems and Applications, Inc., Lanham, MD, USA

Key Points:

- Aurora can be detected in satellite-based Earth nighttime lights using unsupervised machine-learning methods
- A binary aurora mask can be derived and used to eliminate aurora-contaminated nighttime lights observations from analysis for Earth science applications
- These aurora observations can be used for comparison with aurora forecast model predictions and to augment other sources of aurora observations

Correspondence to:
V. Kalb,
virginia.l.kalb@nasa.gov

Citation:
Kalb, V., Kosar, B., Collado-Vega, Y., & Davidson, C. (2023). Aurora detection from nighttime lights for Earth and Space Science applications. *Earth and Space Science*, *10*, e2022EA002513. https://doi.org/10.1029/2022EA002513

Received 18 JUL 2022
Accepted 23 DEC 2022
Corrected 31 JAN 2023

This article was corrected on 31 JAN 2023. See the end of the full text for details.

Author Contributions:

Conceptualization: Virginia Kalb, Burcu Kosar, Yaireska Collado-Vega
Data curation: Virginia Kalb, Burcu Kosar, Yaireska Collado-Vega, Carol Davidson
Formal analysis: Virginia Kalb
Funding acquisition: Virginia Kalb
Investigation: Virginia Kalb, Burcu Kosar
Methodology: Virginia Kalb, Burcu Kosar

Abstract This research leverages data from the Day/Night Band (DNB) of the Visible Infrared Imaging Radiometer (VIIRS) instrument onboard the Suomi National Polar-orbiting Partnership (S-NPP) satellite. We demonstrate the value of mining the VIIRS DNB for aurora and describe our use of unsupervised machine learning to create a binary mask for aurora occurrence. This mask can be used to flag aurora-contaminated observations for NASA's nighttime lights products for Earth science applications. The identification of auroral regions can also be used for Space Weather applications, for example, for comparison with aurora forecast model and with other satellite- or ground-based aurora observations. The DNB is a broadband channel that is sensitive to wavelengths from 500 to 900 nm, which covers most of the visible light spectrum, and as the name implies, captures light even at night with a sensitivity at the nanowatt level. This band is suitable for aurora observations since the light emitted by the aurora tends to be dominated by emissions from atomic oxygen, resulting in a greenish glow at a wavelength of 557.7 nm, especially at an altitude of 110 km. This study compares the global nighttime derived aurora regions for 17 and 18 March with the NOAA Space Weather Prediction Center's (SWPC) probability product for the St. Patrick's Day geomagnetic storm in 2015. VIIRS sensors are slated to be added to the next generation of polar-orbiting operational satellites. Our novel automated approach to aurora identification opens up an efficient way to leverage this unique data source.

1. Introduction

Satellite imagery of the Earth at night reveals both anthropogenic and natural light phenomena. Researchers in Earth science can use nighttime lights as an indicator of human activity, and a proxy for population, economic indicators, energy usage and more (Román & Stokes, 2015). However, more than 20% of the population live in areas where the effects of aurorae present a major challenge in characterizing manmade light sources. Aurora is one of the major ephemeral extraneous light emissions at high latitude (Newell et al., 2014). In this era of concern about global climate change, it is imperative to try to identify and "clean" the nighttime lights signal from this light contamination in pursuit of a consistent long-term record of global energy demand within cities.

Space Weather also has a strong need for knowledge of the aurora as an important visual global indicator of solar-magnetosphere-ionosphere energy transfer during geomagnetic storms. Aurorae are important as these phenomena correlate with highly dynamic Space Weather threats, including GPS scintillations and power grid fluctuations. The irony is that the very signal sought by Space Weather research is noise to the Earth scientists trying to quantify the nighttime lights. We seek to explore this overlap in interests to advance the state of the art for both Space and Earth science through our aurora detection algorithm.

This research leverages data from a polar-orbiting Earth science sensor band that is highly sensitive to visible light, namely the Day/Night Band (DNB) of the Visible Infrared Imaging Radiometer (VIIRS) instrument onboard the Suomi National Polar-orbiting Partnership (S-NPP) satellite (VIIRS Land). This sun-synchronous data source can provide high temporal and spatial resolution observations of the aurora, which can augment current Space Weather data. This data can be compared with aurora forecast models and derived products, hence providing model/product validation and insights into spatially explicit auroral activity in response to the solar wind. Our case study focuses on the Saint Patrick's Day Geomagnetic Storm of 2015. This storm occurs near a new moon, a current prerequisite for our algorithm.

VIIRS DNB has been shown to visually capture the aurora in addition to many other natural and anthropogenic phenomena (Hillger et al., 2014; Miller et al., 2013), and to capture auroral activity during geomagnetic storms

Project Administration: Virginia Kalb
Software: Virginia Kalb, Carol Davidson
Validation: Virginia Kalb, Burcu Kosar
Visualization: Virginia Kalb
Writing – original draft: Virginia Kalb, Burcu Kosar, Yaireska Collado-Vega
Writing – review & editing: Virginia Kalb, Burcu Kosar, Yaireska Collado-Vega

(Shao et al., 2015, 2016). This work goes beyond imagery to scientific data analysis aimed at demonstrating the potential of using DNB data as an authoritative source of auroral activity.

Our focus is to compare aurora forecast model predictions with DNB data. We recognize that the DNB-derived aurora will have uncertainties due to its absence of the red end of the visible spectrum, dependency on the definition of an auroral region for the machine-learning algorithm, and the fact that the OVATION Prime model is based on particle precipitation. However, the citations referenced in the preceding paragraph demonstrate the utility of the VIIRS DNB for aurora observations. The evaluation and validation of Space Weather predictions are critical for forecasters, users, modelers, and stakeholders to identify strengths and weaknesses of each forecast product and facilitate product improvement (Morley, 2020). However, in situ measurements are sparse, so an additional data source could be helpful, as we shall demonstrate. Byproducts of this effort are visualization of fine-grained structure of the aurora in the DNB data, comparison of DNB intensity with solar wind data, and an algorithm for the creation of an aurora mask for use with Earth science studies.

2. Background

2.1. Signal

The near-Earth space environment is constantly bombarded by streams of plasma particles ejected from the Sun that can couple with plasma tied to Earth's magnetic field. Ultimately, at the end of multi-stage processes, this energy is transferred to magnetospheric particles which can cascade down to Earth's upper atmosphere, leading to auroral formation. The result of this complex Sun-Earth system, the aurora, has a visible impact on life and society. The accurate specification of spatial and temporal variations of auroral precipitation patterns in response to a geomagnetic storm would enable improved understanding of the magnetically coupled Sun-Earth system.

Aurora research using visible/infrared imaging from satellites is well documented in literature, beginning with DMSP-2 photographs (Akasofu, 1974). The Reimei satellite, launched in 2005, has a three-channel camera system and top-hat type electron and ion energy spectrum analyzers to simultaneously observe the spatial and temporal dynamics of the auroral fine structure. The camera system captures an image of aurora at three wavelengths: 427.8 (N2+ first negative band), 557.7 (O green line), and 670.0 nm (N2 first positive band) (Obuchi et al., 2008). In their study, Obuchi et al. (2008) found that the auroral emissions of 557.7 and 670 nm are seen in data above the surface of the earth throughout this period, while there are few 427.8 nm emissions, supporting the suitability of VIIRS DNB for aurora observations. Pulsating aurora events have been studied using Reimei data (Nishiyama et al., 2011), and wavelet analysis has been applied to examine vorticity, using motion vectors derived from Reimei optical data (Chaston et al., 2010). The Enhanced Polar Outflow Probe (e-POP) is one of two instrument suites onboard the Canadian satellite CASSIOPE, launched in 2013 (Yau & James, 2011). The primary objective of e-POP is to investigate polar outflow and the associated microscale ion acceleration and wave-particle interactions with auroral excitation. Onboard e-POP is the Fast Auroral Imager (FAI) with two charge-coupled device (CCD) cameras, one for the 630 nm emission of atomic oxygen in aurora and nightside airglow while the other for prompt auroral emissions in the 650–1,100 nm range. This data was used for imaging of auroral pulsations (Lui et al., 2014). These studies rely on photographic interpretation for aurora identification, whereas we propose an automated machine-learning approach for aurora identification.

Aurora can also be imaged from the ground. The Time History of Events and Macroscale Interactions during Substorms (THEMIS) All-Sky Imager (ASI) network observes the aurora within the northern part of the continental United States. Images obtained from space and ground provide better morphological details than the model predictions. The question of whether there is auroral activity in an ASI image has been addressed in the literature. For example, images have been categorized according to auroral type using spatial texture-based methods (Wang et al., 2010). Automatic auroral detection in ASI data has been used to classify images as aurora, non-aurora, or cloudy (Rao et al., 2014). Numeric features for aurora detection have been used for aurora/non-aurora classification (Syrjasuo & Partamies, 2012). All of these studies classify the image as a whole and require manually labeled data. In contrast, our method identifies specific auroral activity within the image, and is unsupervised, hence does not require labeled data. The DNB-identified auroral data offers morphological detail and global coverage that can complement THEMIS ASIs along with legacy DMSP observations. The improved knowledge of auroral specification will provide significant feedback to model predictions, improving the Space Weather knowledge. Our automated approach to aurora feature detection using machine learning is key to the usability of the DNB data in this capacity.

Aurora prediction is extremely complex and the data-starved field of Heliophysics needs an innovative approach for improving Space Weather prediction. Empirical auroral precipitation models do not fully capture small scales and effects of substorms. The time-based approach for combined VIIRS DNB data offers an opportunity for continuous global coverage of the aurora, yielding data on the spatial structure and evolution of a geomagnetic storm. We will compare VIIRS DNB aurora observations with the global probability predictions based on the OVATION Prime 2013 aurora forecast model (Newell et al., 2014), enabling an assessment at the prediction accuracy of the NOAA Space Weather Prediction Center's (SWPC) probability product. We recognize that this assessment is dependent upon the aurora definitions for both data sources, and differences are to be expected. Nevertheless, we think that it is informative for both VIIRS DNB and the NOAA product to compare and contrast observation and prediction.

2.2. Noise

Nighttime lights remote sensing imagery offers a view of the Earth's surface that is unique in that the presence of light is almost entirely due to human activity. There are numerous applications for this type of data:

- Stable city lights, indicative of human population, and a proxy for economic indicators and energy usage,
- Unstable sources such as shipping fleets, gas flares, fires, and the aurora.

The DNB on the VIIRS instrument onboard S-NPP is extremely sensitive, capable of detecting low light with a specified lower limit (L_{min}) of 3 nW (Geis et al., 2012). Post-processing to remove stray light contamination improves upon this pre-launch specification (Liao et al., 2013). However, this sensitivity can only be exploited with high confidence if noise contamination can be mitigated. One such source of noise is the Earth's aurora in high latitude regions. The polar orbit of the S-NPP satellite results in daily coverage of the Earth, with increasing orbital overlap nearing the poles. This orbit yields multiple observations per day in these regions: ranging from about 4 to 10 observations from 60 to 70° per day and about 10–14 observations from 70 to 85°. These multiple daily observations offer a sub-daily temporal frequency of nighttime lights data. This data can be used in Earth science research to track anthropogenic activity in the Arctic, which is changing due to global warming and its disproportionate effect on the Arctic climate. We have a vicious circle, where rising temperatures cause the ice to melt, then the oceans absorb more sunlight and heat up, thus accelerating the warming effect on the planet. As a result, more human activity is occurring, along with light pollution that affects animal and marine life. The Arctic region is especially vulnerable, and nighttime lights could help track changes in population, infrastructure, transportation, and marine activity as the warming climate attracts development. This is a prime use case for nighttime lights to monitor these effects, but the aurora makes it difficult to differentiate light sources. However, aurora being confined to a high latitude region makes it especially amenable to the multiple observations available with a time-based product.

Figure 1 shows a portion of the DNB over northern Russia before (a) and during the St. Patrick's Day storm (b). The aurora totally overwhelms the nighttime lights from urban activity during the geomagnetic storm.

Thus, the aurora is noise for Earth science, but signal for Space science, and both disciplines can benefit from auroral identification. As noted in the previous section, the DNB observations can help improve the knowledge of the auroral activity during a geomagnetic storm. Therein lies the synergy between Earth science and Space Weather.

2.3. St. Patrick's Day Storm

A C-class solar flare originating from the southwest region of the solar disk that peaked around 15 March 2015 T02:13Z was associated with a fast coronal mass ejection (CME) and a solar energetic particle event. The average speed of the CME was around 670 km/s and it arrived at Earth on 17 March 2015. Before the CME arrival, solar wind monitors detected a shock associated with a coronal hole high speed stream that arrived the day before on 16 March 2015. The disturbance caused by this combination of events caused a strong geomagnetic storm (Kamide & Kusano, 2015). The Kp index (an index that measures the disturbance on the Earth's magnetic field from 0 to 9, 9 being the highest intensity (Kp) reached values of Kp = 8 on 17 March 2015) (Figure 2). These are favorable conditions for intense auroral formation. Aurora sightings were reported from Minnesota, Wisconsin, both North and South Dakota, Washington State and Alaska. The solar wind conditions shown in Figure 3 are from the

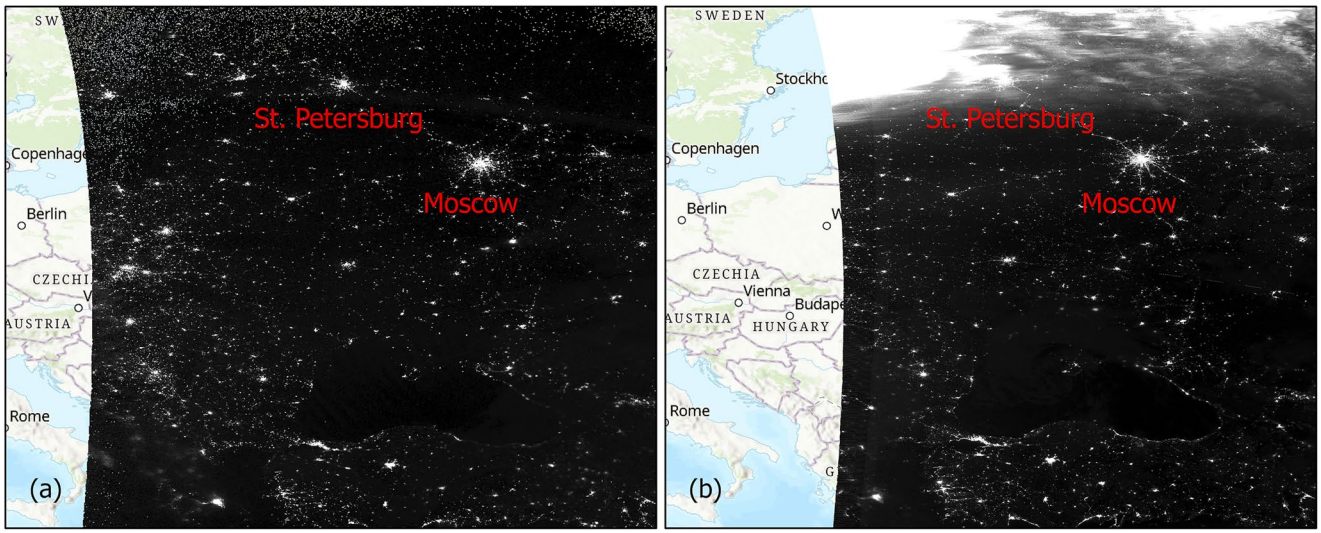

Figure 1. The image on the left, acquired on 16 March 2015 23:00–23:12 UT, clearly shows nighttime lights in northern Russia. The right-hand image, acquired on 17 March 2015 at 23:12–23:24 UT, is obscured by the aurora.

multi-spacecraft OMNI data set (solar wind data shifted to the Earth's bow shock) (King & Papitashvili, 2005). It shows the shock caused by the CME arrival on 17 March with the solar wind speed, the total magnetic field magnitude B, the z component of the magnetic field B_z, and the Auroral Electrojet (AE) index which is derived from geomagnetic variations and defines the overall activity of electrojets within the auroral oval. Nominal values are 5 nT for the magnetic field magnitude and 400 km/s for the solar wind speed. Looking at Figure 3, the shock seems to arrive around 17 March 2015 T04:05Z where there is a sharp increase in both values. The strong geomagnetic storm following the shock arrival is strongly correlated to the highly negative value of the B_z component. The higher value of the B_z southward component, the higher the erosion of the dayside magnetosphere, leading to a stronger geomagnetic storm. The solar wind conditions are available as high resolution (5 min averaged) variables from NASA/GSFC's OMNI 5 min data set through the OMNIWeb interface (Papitashvili & King, 2020).

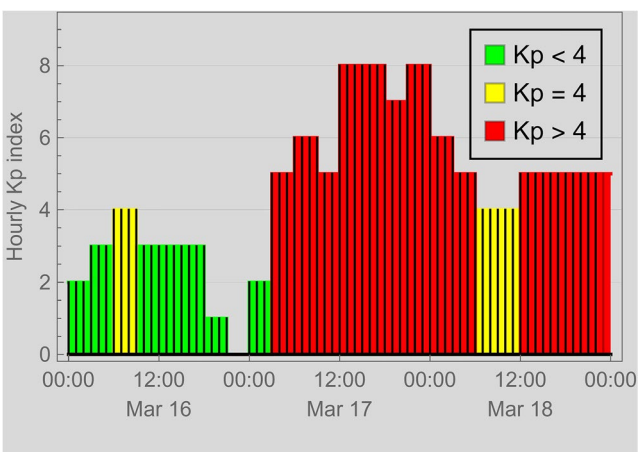

Figure 2. The Kp index over the three days starting March 16 shows the evolution of the geomagnetic storm with red bars indicating high activity. The times shown are UTC at the height of the storm.

3. Data

3.1. DNB

The Visible Infrared Imaging Radiometer Suite (VIIRS) is a key instrument onboard the Suomi-National Polar-orbiting Partnership (S-NPP) satellite, which collects data in multiple wavelengths at nadir resolutions of 375 and 750 m, including a unique low-light imaging channel known as the Day/Night band (DNB). While nighttime lights have been observed from the Defense Meteorological Satellite Program Operational Linescan System (DMSP OLS), the VIIRS DNB improves upon this spatially and radiometrically—DMSP OLS is quantized to 8 bits, and suffers from saturation with bright targets. The VIIRS DNB onboard calibrated radiance presents a new capability for quantitative research with its dual gain, floating point format, and offers opportunities to explore new applications for nocturnal low-light phenomena such as aurora (Miller et al., 2013). The VIIRS DNB has a near constant footprint of 750 m across its ~3,000 km wide swath. Its spectral response is 0.5–0.9 μm (visible/near-infrared) and novel time-delay integration provides high sensitivity to low-light conditions.

3.2. OVATION Prime 2013 Model Data

Auroral oval predictions are generally based on data collected by various space-based particle detectors or imagers and their incorporation into

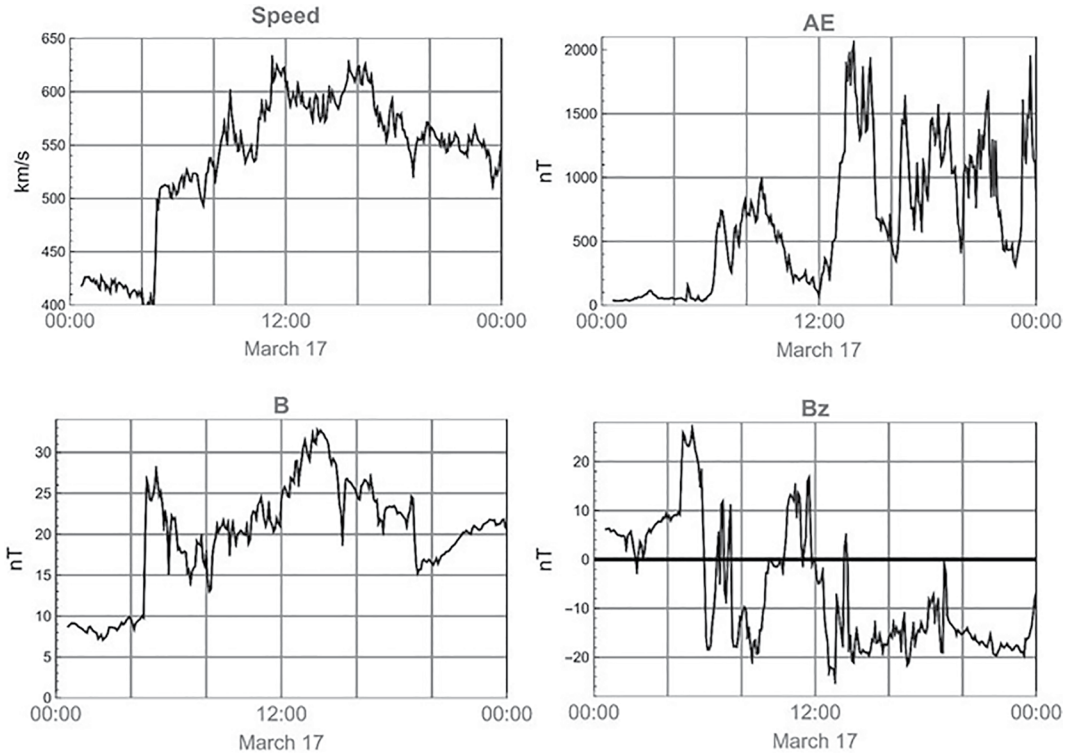

Figure 3. Solar wind conditions at the onset of the St. Patrick's Day storm. Its arrival around 04:00 UT on 17 March 2015 is reflected in the sharp increase in speed and magnetic field magnitude, and the abrupt reversal of the *z* component of the magnetic field. The AE-index reflects the intensification of the storm.

empirical models that make predictions of the precipitation patterns in the high latitude regions of the Earth. OVATION Prime 2013 (OP-13) is an auroral precipitation model (Newell et al., 2014) that uses in-situ particle measurements by SSJ4/5 detectors onboard DMSP and a highly accurate solar wind-magnetosphere coupling function (Newell et al., 2007) to produce high resolution energy flux maps between 50° and 90° magnetic latitude in both hemispheres. This coupling function is highly dependent on the solar wind conditions measured at Earth's first Lagrangian point (L1) that is located about a million miles (1.5×10^6 km) upstream on the Sun-Earth line. When calculating auroral precipitation, this model accounts for different auroral types and seasonal variations which ensures its accuracy of modeling the auroral oval better in comparison to other real-time models. However, DMSP satellites have insufficient data in the post-midnight region due to their sun-synchronous orbits. To compensate for this OP-13 performs interpolation across this gap (Newell et al., 2014). In comparison to earlier versions of the model which are limited due to lack of data for very active times, the OP-13 model is improved to overcome this limitation by using Global Ultraviolet Imager (GUVI) total energy flux data in conjunction with particle data (Newell et al., 2014).

The operational implementation of OP-13 model at NOAA's Space Weather Prediction Center (SWPC) generates a product for the percent probability of visible aurora at a cadence of 30 min (https://www.swpc.noaa.gov/products/aurora-30-minute-forecast). This operational product first converts the OP-13 model output from geomagnetic to geographic coordinates and then resamples into an array of 1,024 bins in longitude and 512 bins in latitude (which leads to about 0.35° resolution in both latitude and longitude). The percent probability of visible aurora is obtained by assuming a linear relationship to the auroral flux.

The OP model's ability to predict the location and intensity of the auroral oval have been validated by many studies (Kosar et al., 2018; Lane et al., 2014; Machol et al., 2012; Mitchell et al., 2013; Newell et al., 2010), however, little extensive testing has been performed on the accuracy of NOAA's Space Weather Prediction Center's (SWPC) forecast product, the percent probability of visible aurora. Case et al. (2016) evaluated this product against citizen science reports. Recently (Mooney et al., 2021), the performance of this product was evaluated by comparing forecast outputs with the location of the auroral oval from IMAGE FUV instruments. This work aims to perform a case study to globally compare this product with VIIRS DNB.

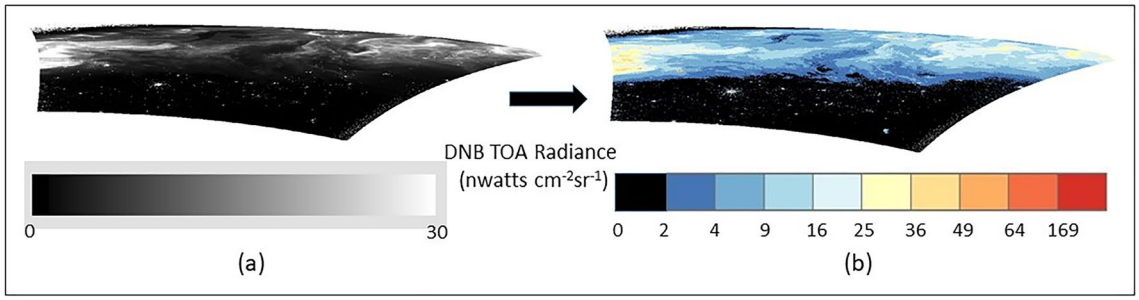

Figure 4. Panel (a) shows the raw DNB radiance for a sample swath with the aurora present, (b) shows the pre-processed data, with a non-linear mapping to 10 bins and filtered by solar zenith angle, which removes a bit of the upper right corner of the swath due to possible stray light contamination. Data is displayed in cylindrical equal area projection, the default unless otherwise specified.

4. Methods

4.1. Data Acquisition

The DNB data level 1 data products VNP02DNB<>.nc (top of atmosphere radiance) and VNP03DNB<>.nc (geolocation) are freely available from the Level-1 and Atmosphere Archive and Distribution System (LAADS) Distributed Active Archive Center (DAAC) via the EarthData portal (https://earthdata.nasa.gov/), and were acquired for days 17 and 18 of March 2015. These are 6 min granules, so 480 datasets were needed at about 100 Mbytes/data set. Data resolution is 750 m at nadir, and is nearly constant across the swath. The VNP03DNB product contains latitude and longitude arrays geolocating the center of each pixel on the surface of the Earth. The geolocation algorithm uses Earth ellipsoid and terrain surface information in conjunction with spacecraft (S/C) ephemeris and attitude data, and knowledge of the VIIRS instrument and satellite geometry to compute geodetic coordinates (latitude and longitude), height, ground to satellite direction and range, and solar and lunar vectors (Geolocation ATBD). However, the aurora is brightest around 100–110 km above the Earth. For a comparison of spatially located aurora with the Ovation Prime data, we need to adjust for the parallax effect of the aurora at 110 km. We modified the geolocation code and recomputed the geolocation for days 17 and 18 using an inflated Earth to get the DNB radiance at the aurora height which we then used to project the data. This product also has

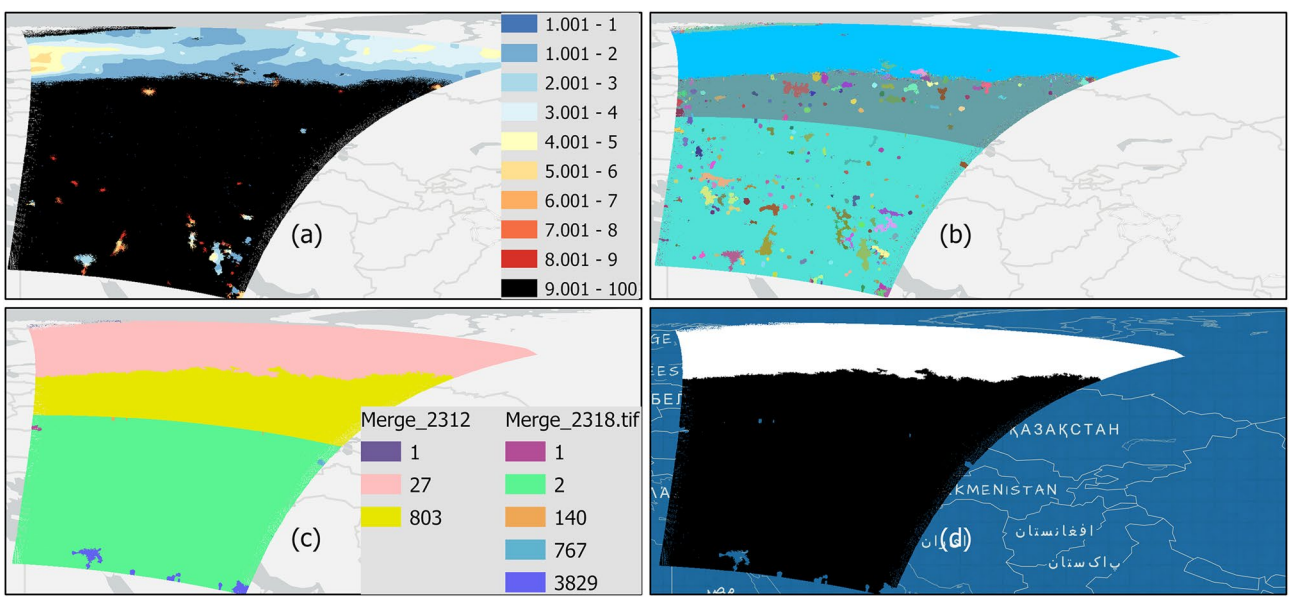

Figure 5. Workflow for deriving binary aurora/non-aurora mask from the DNB radiance: (a) smoothing, (b) mean shift segmentation, (c) filtered by area and underlying statistics, (d) final binary mask. Results are shown for 17 March, 6 min granules commencing at 23:12 and 23:18.

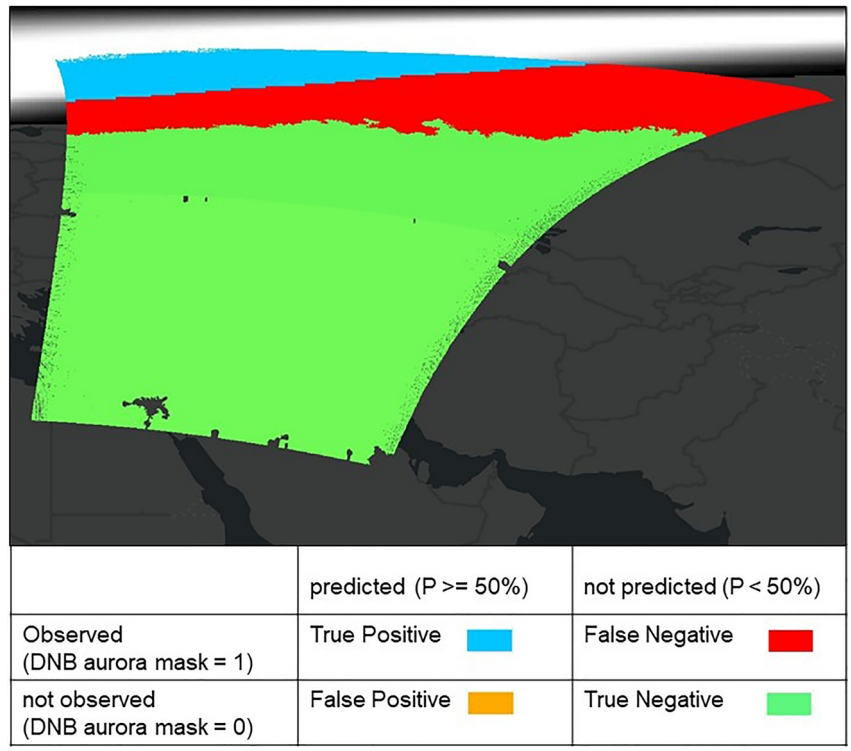

Figure 6. Shown are values based on aurora probability (*P*) and DNB-derived aurora presence. The temporally closest aurora forecast is shown as background to the classified granule. No comparison is done when the mask value is NODATA, as shown in the small regions on the border of granule 23:18 UT since they fall the size minimum but were missed by the small region merging tool.

the solar zenith angle which is needed to filter the data. The radiance values are in floating point format in watts/(cm^2-sr).

We have NOAA's model, identical to that used by the SWPC to generate forecast probabilities. Our only modification is to run it at a 15 min cadence. The linear scaling is done by the model. The OVATION Prime aurora forecast model was initialized with the solar wind parameters corresponding to the period of the onset of the geomagnetic storm. Global maps were produced in ASCII format. These maps are in geographic projection with a data resolution of 0.30.35° × 1°. The model output represents percent probability of aurora occurrence. The files are converted to geotiff format for this study.

4.2. Data Wrangling

Nighttime DNB granules are selected by reading the Day/Night flag metadata. Further filtering of the DNB files by solar zenith angle ≥102° eliminates stray light contamination. The data is scaled to nanowatts and gridded to the Cylindrical Equal Area projection at 5 km resolution in geotiff format. The large dynamic range (several orders of magnitude) of the DNB means that any linear scale will fail to reveal detail at both dim and bright light sources. Thus, a square root transform is applied to the data, followed by assigning an integer data value from 1 to 9 according to the following breakpoints 2, 4, 9, 16, 25, 36, 49, 64, 169 which is close to a linear mapping at the low end for the transformed data. This product will subsequently be referred to as binned DNB data. We initially performed the analysis using a lower limit of 3, but found that it missed some regions that visually did represent the aurora, so we ultimately used a lower threshold (L_{min}) of 2 nW. This is justified by the improved performance of the DNB with the stray light correction (Liao et al., 2013) and by our strict filtering by solar zenith angle.

This step facilitates visual interpretation, but more importantly is critical to the analysis. Values below the 2 nW threshold are mapped to value of 10 for subsequent processing. This serves to distinguish the background from the aurora, which tends to have lower radiance values. Figure 4 shows the raw DNB radiance and the binned

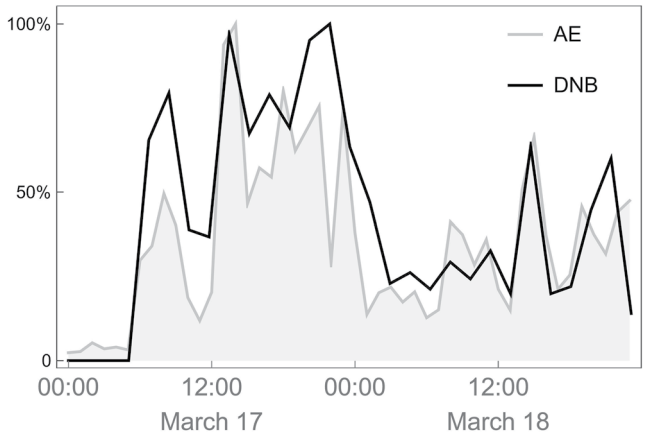

Figure 7. The solid black line indicates a normalized count of aurora-classified pixels, binned by orbit. The gray line is the normalized AE index, with the area under the curve filled for better visual comparison.

DNB data for the granule from 17 March 2015, 23:12 UT. This granule and the next at 23:18 UT will be used in subsequent graphics demonstrating the aurora mask creation.

4.3. Data Analysis

The primary task for a comparison between the aurora probability product and the DNB data is to create an aurora binary mask for the DNB observations. A challenge for aurora detection is the overlap that exists between radiance levels of the aurora and anthropogenic nighttime lights. However, aurora phenomena exhibit a coherent structure that is distinct from the spatial signature of human settlements. The amorphous cloud-like spatial extent is difficult to define; hence, we turn to machine learning methods to learn spatial patterns and statistical properties of the aurora. Image segmentation can separate the aurora from anthropogenic light sources, and can automate this process for production-level processing. This was implemented using the mean shift segmentation method (Cheng, 1995) that groups adjacent pixels that have similar spectral and spatial characteristics. Run-time parameters allow the weighting of spatial and spectral smoothing to customize the algorithm to features of interest. Our methodology quantifies the spatial extent properties of the aurora in two ways: aurora regions must be larger than 4,000 pixels, and their DNB region average must be less than a pre-determined value of 50. This value has been determined by visual inspection, and has only been tested on near new moon conditions, which is the case for the St. Patrick's Day storm. This heuristic is derived from observing that the DNB radiance values for auroral regions are lower than that of human settlements. This workflow is implemented using tools from the Orfeo Toolbox, an open source project for remote sensing (Grizonnet et al., 2017).

Since the workflow depends upon an area measurement, both the DNB data and the aurora probability snapshots are projected to the Cylindrical Equal Area. The heart of the workflow is the segmentation of the DNB data. We previously assigned a binned value of 10 for DNB data below the minimum threshold. For subsequent processing, we assign a value of 100 to those pixels to really distinguish background data from valid DNB data. Then the data is smoothed using Orfeo's MeanShiftSmoothing with a spatial radius of 10 and a range radius of 9. Application of this step to our sample granule is shown in Figure 5a for 17 March, granules 23:12 and 23:18. Next we apply the LSMSSegmentation tool with a spatial radius of 15 and a range radius of 3. This step delineates the major features, but also identifies small segments around anthropogenic light sources (Figure 5b). Orfeo's SmallRegionsMerging tool with a minimum size of 4,000 pixels to merge small regions with an adjacent larger and radiometrically similar region, leaving large segments (Figure 5c). However, this tool fails to merge small segments that are adjacent to the border, as evidenced in granule 23:18, so these regions are identified and set

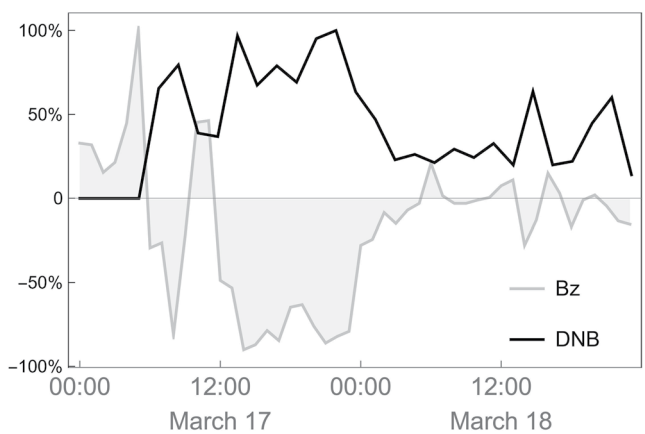

Figure 8. The solid black line indicates a normalized count of aurora-classified pixels, binned by orbit. The gray line is the normalized B_z component of the magnetic field, with the area under the curve filled for better visual comparison.

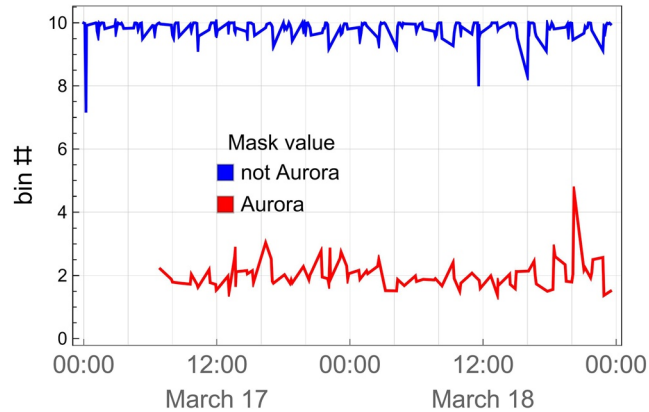

Figure 9. The mean values for the aurora regions correspond to our assertion that the DNB binned values are lower in those regions than for non-aurora regions. This separation is possible because our thresholding step helps to associate urban regions with their surrounding non-aurora regions, creating large non-aurora regions with high mean values.

to NODATA. Finally, to determine whether a segment identifies an auroral region or not, the statistics of each segment are computed. If the mean exceeds a pre-determined value of 50, it is classified as non-aurora, and the mask value is set to 0. Otherwise, the mask value is set to 1, identifying the aurora (Figure 5d). A threshold value of 50 corresponds to classifying a segment that is more than 50% background (below L_{min}) as non-aurora when mapping background values to 100.

Using this workflow, all granules for 17 and 18 March 2015 were processed to derive a granule-level aurora mask. For each granule, the nearest aurora probability forecast was identified, and intersected with the aurora mask. Agreement between forecast and observation occurs if either the mask equals 1 and the forecast probability is greater or equal to 50%, or if the mask equals 0 and the forecast probability is less than 50%. These cases are termed true positive and true negative, respectively. The remaining cases are where forecast and observation disagree. These cases are illustrated in Figure 6 for the sample granules from 17 March, 23:12 UT and 23:18 UT with a background of the closest aurora probability forecast at 23:15 UT. The forecast probability is represented by a grayscale ranging from 0 (black) to 100% (white).

5. Discussion

Given the temporal and spatial sampling of the DNB of the globe, one question we can address is the ability of the DNB to track auroral activity in time. To this end, we constructed a DNB time series which counts pixels classified as aurora during an orbit. This temporal aggregation is necessary since many granule-level time steps would be over mid-latitude regions and would not be a global measure of auroral activity. We normalized this time series and compared it to the normalized hourly AE index (Figure 7) and the normalized hourly z component of the magnetic field, B_z (Figure 8). The DNB-derived time series of auroral activity roughly captures the peaks in AE index, especially during the most active period of the storm. This aligns with Shao et al. (2016) who also found correlation between DNB radiance and the AE index. The DNB-derived time series shows an inverse correlation with negative B_z, As mentioned previously, the higher value of the B_z southward component, the higher the erosion of the dayside magnetosphere, leading to a stronger geomagnetic storm, and the DNB activity index captures this dynamic.

Given that we depend upon the automatic segmentation to derive the aurora mask and subsequent comparison with the aurora data, it is important to quantify how well this methodology works. The premise is to separate large segments with low binned values from large segments with high binned values, with the underlying assumptions that the auroral regions will be relatively large compared to urban regions. We derived the mean values for aurora regions and for non-aurora regions for every granule to test this separation. The results, shown in Figure 9, confirm that the segmentation has successfully separated the aurora and non-aurora regions. Our thresholding step is critical to enabling this separation, by assigning a large value to the dark regions surrounding urban centers.

10.1029/2022EA002513

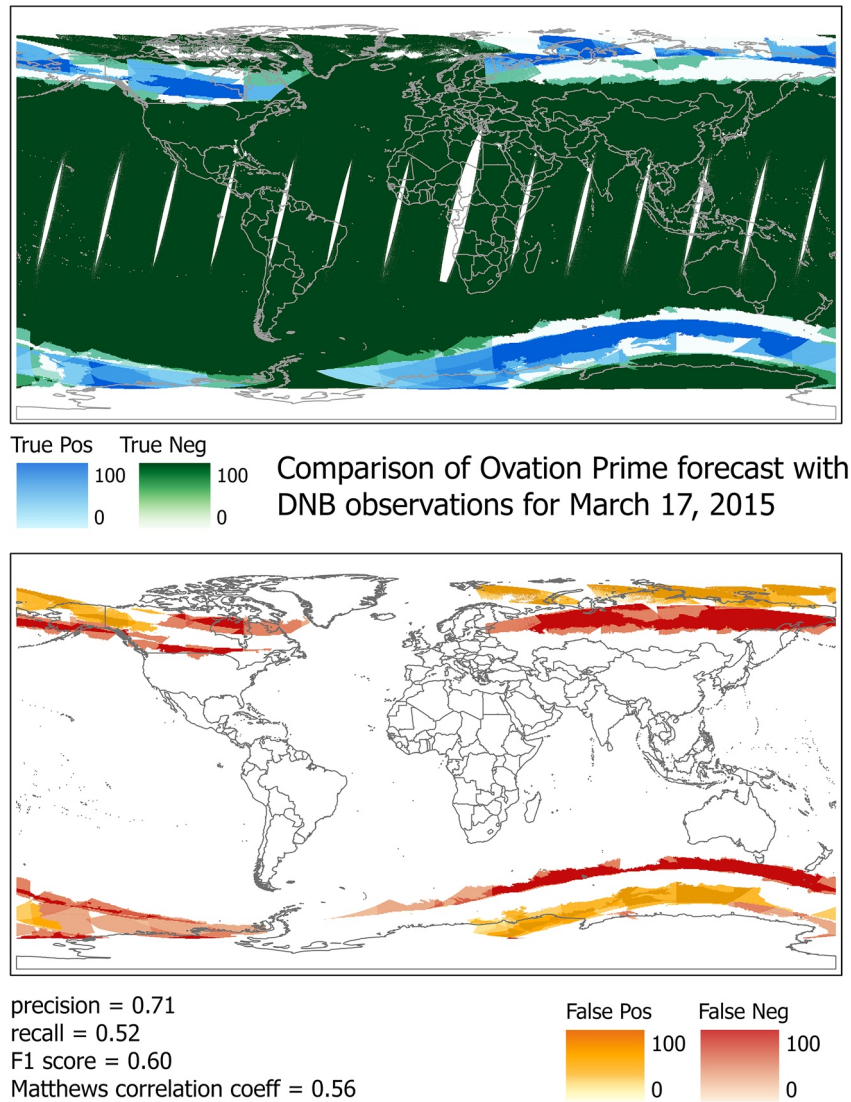

Figure 10. Comparison of predicted aurora with DNB observations for 17 March 2015 by the statistics measuring agreement and disagreement between predicted and observed. There are gaps in equatorial coverage because we have elevated the observations to 110 km above the Earth to match the average aurora height.

Several statistics can be derived from the comparison of DNB observation and forecast by summing each outcome type over all grid cells, normalized by the total count:

$$\text{precision} = \text{True Positive}/(\text{True Positive} + \text{False Positive})$$

$$\text{recall} = \text{True Positive}/(\text{True Positive} + \text{False Negative})$$

$$\text{F1 score} = 2 \times (\text{Precision} \times \text{Recall})/(\text{Precision} + \text{Recall})$$

$$\text{Matthews Correlation Coefficient} = (\text{TP} \times \text{TN}–\text{FP} \times \text{FN})/((\text{TP} + \text{FP}) \times (\text{TP} + \text{FN}) \times (\text{TN} + \text{FP}) \times (\text{TN} \times \text{FN}))^{½}$$

where True Positive (TP) is observed and predicted, True Negative (TN) is not observed and not predicted, False Positive (FP) is not observed but predicted, and False Negative (FN) is observed but not predicted. The accuracy score ((TP + TN)/(TP + TN + TN + FP)) is misleading given the imbalance between aurora and non-aurora spatial coverage, and is not used as a metric here. The F1 score and Matthews Correlation Coefficient (MCC) (Matthews, 1975) are better suited to this situation.

10.1029/2022EA002513

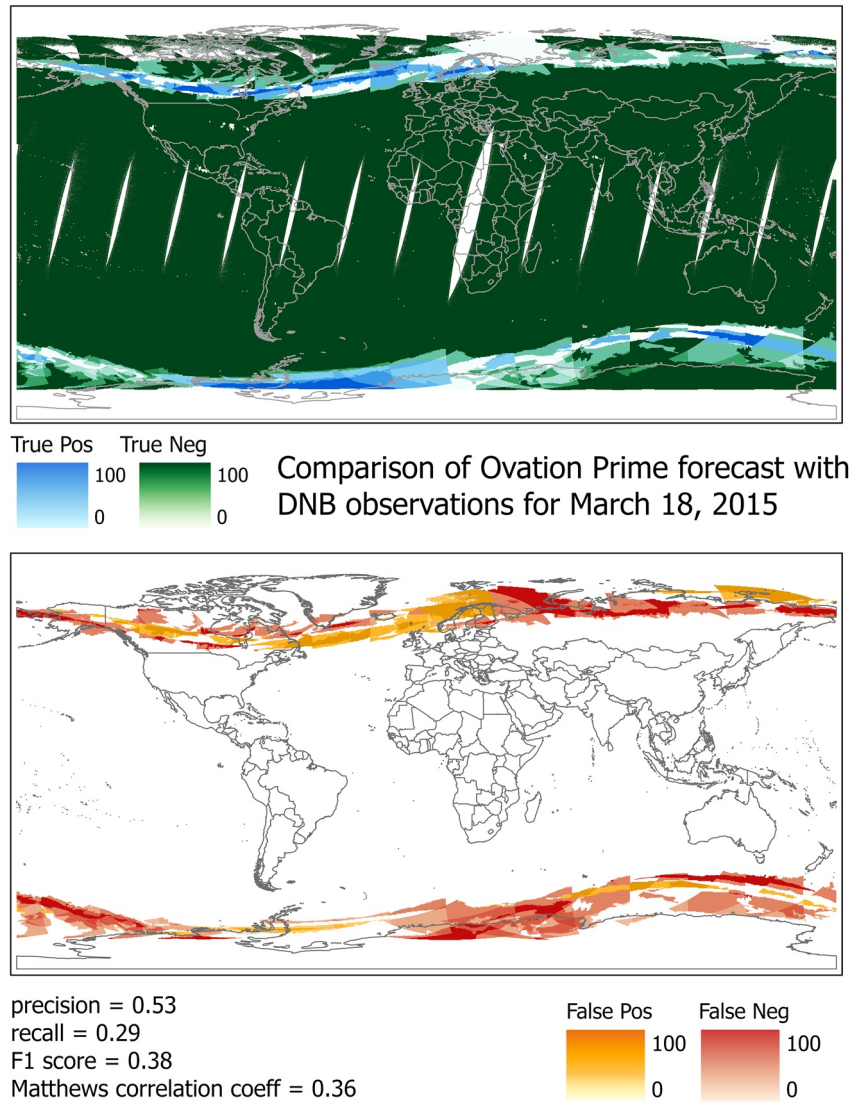

Figure 11. Comparison of predicted aurora with DNB observations for 17 March 2015 by the statistics measuring agreement and disagreement between predicted and observed.

To get a spatially explicit global comparison of the forecast probability and DNB observations, we adopt a strategy similar to the approach that was used by Machol et al. (2012) of creating a global grid and calculating the percentage of observed/predicted pairs of each type (True Positive, *etc*.) out of all observed/predicted pairs for each grid cell, aggregated over a specified time interval. This method takes into account the time-varying nature of both data sources, and the spatial variability of the DNB observations. For our purposes, we aggregate over each day of the storm. Figures 10 and 11 show the results for 17 and 18 March respectively. While the true positives are important as indicative of the product correctly predicting the probability of aurora, the true negatives are equally important. The classification of DNB aurora is only as good as the mask derivation, and it is a good indicator that we don't have low latitude aurora sightings in the DNB observations. Since the DNB takes 24 hr to cover the globe, this comparison is by nature not comprehensive in the sense that we can only compare at the observation times, although we get more frequent observations near the poles.

These figures tell different stories for 17 and 18 March. On 17 March when the aurora activity is strongest, we see observations extending further toward mid-latitude regions than the predictions, and more pole-ward predictions than aurora observations (Figure 10). However on 18 March when the storm is abating, we do not see this pattern. Instead the dominant pattern is false negatives where the aurora is observed but not predicted (Figure 11).

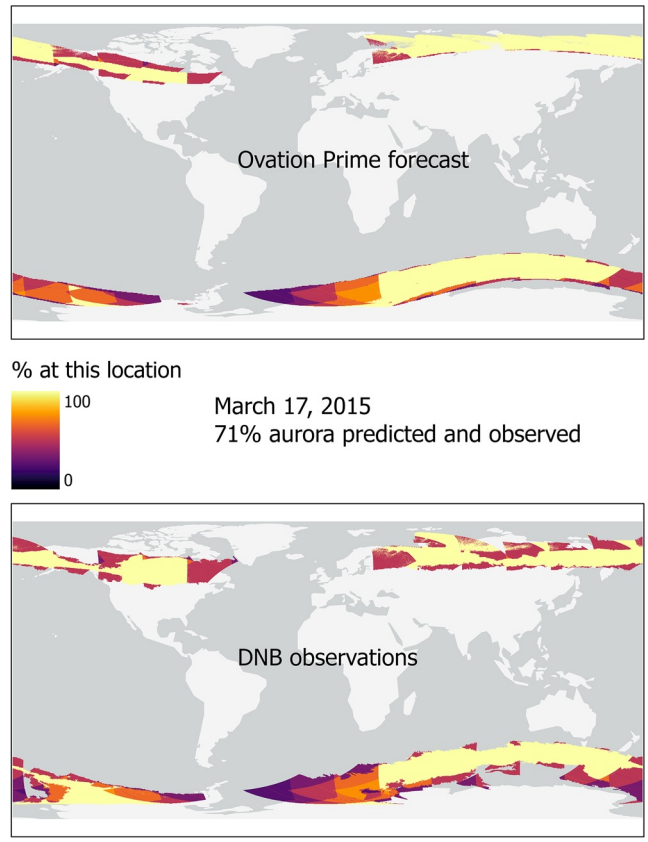

Figure 12. Visualization of all aurora probability forecasts with probability ≥50% (top) and all DNB observations where the binary mask indicates auroral activity (bottom).

Another way of visually comparing probability forecast with observation is shown in Figures 12 and 13, where aurora probability ≥50% (TP + FP) is displayed with the same color scale as observed aurora (TP + FN). The observations for 17 March find auroral activity extending further into the mid-latitudes that are not predicted using the ≥50% probability threshold for the aurora probability product. This threshold is another dependency that impacts the results.

Delving deeper into the lack of agreement between observation and prediction, we can look at the gap in prediction on 18 March near the Southern Ocean, around 46° east, 62° south. Figure 14a shows the DNB radiance for the granule 20:06 UT, scaled from 0 to 10 nW/(cm^2-sr). Figure 14b shows the binned data for this granule. The computed aurora mask is in Figure 14c. This mask is displayed with 30% transparency on top of the nearest aurora prediction at 20:00 UT. With a prediction threshold of 50%, the aurora is not predicted in this region, at odds with the DNB observations.

As mentioned previously, we think that using $L_{min} = 2$ does a better job of finding the aurora in the DNB, and the statistics bear this out. Table 1 compares the scores for 17 and 18 March for $L_{min} = 2$ and $L_{min} = 3$.

6. Conclusion

The DNB offers a unique resource for aurora observations, enabling the comparison between aurora forecast probability predictions with actual observations. Global daily coverage permits a time-sensitive way to track a geomagnetic storm, with near hourly coverage near the poles. To ensure seamless and continuous collection of nightlights data, VIIRS sensors are slated to be added to the next generation of polar-orbiting operational satellites, the Joint Polar Satellite System (JPSS). Since JPSS-1 has already launched, currently there are two VIIRS instruments on orbit today—S-NPP and JPSS-1, which will double the aurora observational capability. Additional VIIRS sensors will be included on JPSS-2, scheduled to launch in 2021, followed by JPSS-3 in 2026, and JPSS-4 in 2031.

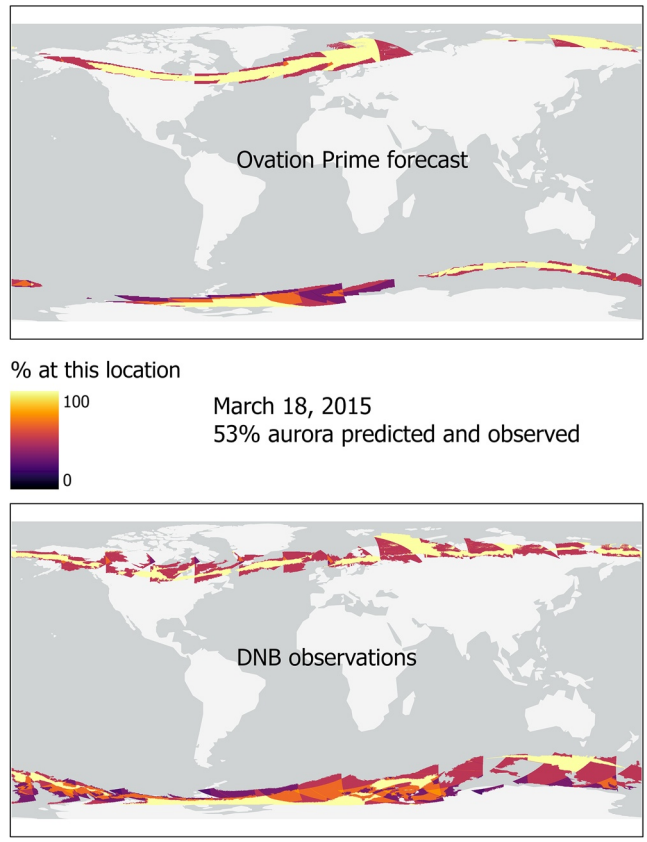

Figure 13. Visualization of all aurora probability forecasts with probability ≥50% (top) and all DNB observations where the binary mask indicates auroral activity (bottom).

The DNB data offers morphological detail and daily global coverage that can complement and advance THEMIS ASIs along with legacy DMSP observations. Space-based auroral observations have an advantage of viewing the aurora above the clouds, although future work will need to adjust the aurora segmentation algorithm to account for moonlit clouds that can be confused with the aurora. Localized aurora can occur anywhere in the polar region with respect to the auroral oval (Frey, 2007), and the DNB observations offer an opportunity to systematically capture this phenomenon.

The improved knowledge of auroral specification will provide significant feedback to model predictions, improving space weather knowledge. This comparison is beneficial to Earth science as well by helping to refine how DNB observations are classified as aurora to avoid misinterpretation as anthropogenic lights. Even though we are currently limited to aurora detection for low lunar fraction, this can benefit temporal composites (*e.g.*, monthly or annual) of nighttime lights.

Space weather prediction faces numerous challenges, including the development of appropriate validation methodologies (Morley, 2020). Currently, many stakeholders rely on the predictions of the aurora forecast model that is disseminated by NOAA's Space Weather Prediction Center (SWPC). This empirical model does not take into account contributions from auroral substorms that are explosive energy storage and release during the progression of a geomagnetic storm. Substorms can cause the auroral oval to change significantly in a much faster temporal scale than any empirical model can predict. Fine resolution aurora data provided by DNB can patch this knowledge gap. The Community Coordinated Modeling Center (CCMC) at NASA GSFC leads model validation efforts that underscore the immediate need for an accurate space weather prediction capability within the community. In the NSF Coupling Energetics and Dynamics of Atmospheric Regions (CEDAR)—Geospace Environment Modeling (GEM) 2016 conference, an ionospheric conductance challenge was introduced to the scientific community. The success of this challenge relies on accurate specification of this parameter and understanding conductance related processes. Auroral precipitation in the high latitude ionosphere is an important physical process affecting

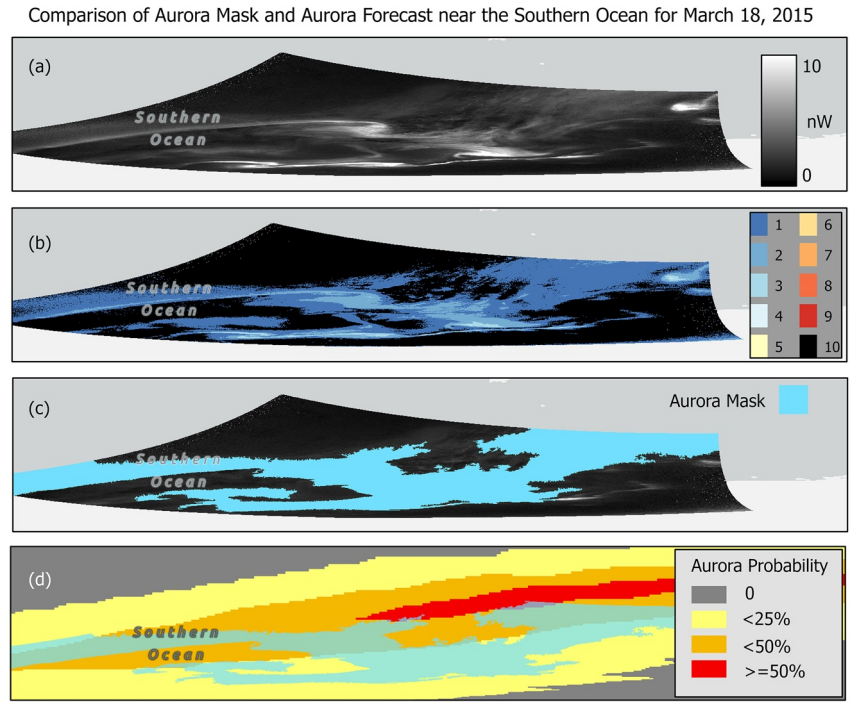

Figure 14. A closer look at a region where observation and prediction disagree. Panel (a) shows the DNB radiance for the granule 20:06 UT, scaled from 0 to 10 nW/(cm^2-sr). Panel (b) shows the binned data for this granule. The computed aurora mask is in panel (c). This mask is displayed with 30% transparency on top of the nearest aurora prediction at 20:00 UT.

Table 1
Performance Metrics Measuring the Agreement and Disagreement Between Aurora Prediction and Observation

17 March 2015	$L_{min} = 2$	$L_{min} = 3$
Precision	0.71	0.56
Recall	0.52	0.53
F1 score	0.60	0.54
Matthews CC	0.56	0.50
18 March 2015		
Precision	0.53	0.31
Recall	0.29	0.32
F1 score	0.38	0.31
Matthews CC	0.36	0.28

the ionospheric conductance. Therefore, improved knowledge of auroral specification will provide important feedback to this challenge.

Data Availability Statement

The projected DNB radiance data scaled to nanowatts, the Ovation Prime geotiffs, and the binary aurora mask geotiffs used in this work have been uploaded to zenodo.org (Kalb et al., 2022).

Acknowledgments
This work was funded through NASA's Science Innovation Fund and NASA Internal Research and Development funds, and NASA's Terra, Aqua, Suomi-NPP, and NOAA-20 program Grant 80NSSC22K0199. Thanks to Robert Wolfe and Guoqing Lin at Goddard Space Flight Center for discussions on how to correct the geolocation for the aurora height.

References

AE. (n.d.). Retrieved from https://www.ngdc.noaa.gov/stp/geomag/ae.html#:~:text=The%20Auroral%20Electrojet%20Index%2C%20AE%2C and%20within%20the%20auroral%20oval

Akasofu, S.-I. (1974). A study of auroral displays photographed from the DMSP-2 satellite and from the Alaska meridian chain of stations. *Space Science Reviews*, *16*(5–6), 617–725. https://doi.org/10.1007/bf00182598

ASI. (n.d.). Retrieved from http://themis.igpp.ucla.edu/instrument_asi.shtml

Case, N. A., MacDonald, E. A., & Viereck, E. R. (2016). Using citizen science reports to define the equatorial extent of auroral visibility. *Space Weather*, *14*(3), 198–209. https://doi.org/10.1002/2015SW001320

Chaston, C. C., Seki, K., Sakanoi, T., Asamulr, K., & Hirahara, M. (2010). Motion of aurorae. *Geophysical Research Letters*, *37*(8), L08104. https://doi.org/10.1029/2009gl042117

Cheng, Y. (1995). Mean shift, mode seeking, and clustering. *IEEE Transactions on Pattern Analysis and Machine Intelligence*, *17*(8), 790–799. https://doi.org/10.1109/34.400568

DMSP. (n.d.). Retrieved from https://ngdc.noaa.gov/eog/dmsp.html

DMSP OLS. (n.d.). Retrieved from https://dmsp.bc.edu/html2/dmsp_ols.html

Frey, H. U. (2007). Localized aurora beyond the auroral oval. *Reviews of Geophysics*, *45*(1), RG1003. https://doi.org/10.1029/2005RG000174

FUV. (n.d.). Retrieved from http://sprg.ssl.berkeley.edu/image/

Geis, J., Florio, C., Moyer, D., Rausch, K., & De Luccia, F. J. (2012). VIIRS day-night band gain and offset determination and performance. *Earth Observing Systems XVII* (Vol. 8510, pp. 399–48). SPIE.

Geolocation ATBD. (n.d.). Retrieved from https://ladsweb.modaps.eosdis.nasa.gov/missions-and-measurements/viirs/NASARevisedVIIRSGeolocationATBD2014.pdf

Grizonnet, M., Michel, J., Poughon, V., Inglada, J., Savinaud, M., & Cresson, R. (2017). Orfeo ToolBox: Open source processing of remote sensing images. *Open Geospatial Data, Software and Standards*, *2*(1), 15. https://doi.org/10.1186/s40965-017-0031-6

GUVI. (n.d.). Retrieved from http://www.timed.jhuapl.edu/WWW/mission/instruments/GUVI.php

Hillger, D., Seaman, C., Liang, C., Miller, S., Lindsey, D., & Kopp, T. (2014). Suomi NPP VIIRS imagery evaluation. *Journal of Geophysical Research: Atmospheres*, *119*(11), 6440–6455. https://doi.org/10.1002/2013jd021170

IMAGE. (n.d.). Retrieved from https://image.gsfc.nasa.gov/

Kalb, V., Kosar, B., Collado-Vega, Y., & Davidson, C. (2022). Aurora detection from nighttime lights for Earth and Space Science applications [Dataset]. Zenodo. https://doi.org/10.5281/ZENODO.6527483

Kamide, Y., & Kusano, K. (2015). No major solar flares but the largest geomagnetic storm in the present solar cycle. *Space Weather*, *13*(6), 365–367. https://doi.org/10.1002/2015sw001213

King, J. H., & Papitashvili, N. E. (2005). Solar wind spatial scales in and comparisons of hourly Wind and ACE plasma and magnetic field data. *Journal of Geophysical Research*, *110*(A2), A02104. https://doi.org/10.1029/2004ja010649

Kosar, B. C., MacDonald, E. A., Case, N. A., Zhang, Y., Mitchell, E. J., & Viereck, R. (2018). A case study comparing citizen science aurora data with global auroral boundaries derived from satellite imagery and empirical models. *Journal of Atmospheric and Solar-Terrestrial Physics*, *177*, 274–282. https://doi.org/10.1016/j.jastp.2018.05.006

Kp. (n.d.). Retrieved from https://auroraforecast.is/kp-index/

Lane, C., Acebal, A., & Zheng, Y. (2014). Assessing predictive ability of three auroral precipitation models using DMSP energy flux. *Space Weather*, *13*(1), 61–71. https://doi.org/10.1002/2014sw001085

Liao, L. B., Weiss, S., Mills, S., & Hauss, B. (2013). Suomi NPP VIIRS day-night band on-orbit performance. *Journal of Geophysical Research: Atmospheres*, *118*(22), 12705–12718. https://doi.org/10.1002/2013jd020475

Lui, A. T. Y., Cogger, L. L., Howarth, A., & Yau, A. W. (2014). First satellite imaging of auroral pulsations by the Fast Auroral Imager on e-POP. *Geophysical Research Letters*, *42*(17), 6877–6882. https://doi.org/10.1002/2015gl065331

Machol, J. L., Green, J. C., Redmon, R. J., Viereck, R. A., & Newell, P. T. (2012). Evaluation of OVATION Prime as a forecast for visible aurorae. *Space Weather*, *10*(3), S03005. https://doi.org/10.1029/2011SW000746

Matthews, B. W. (1975). Comparison of the predicted and observed secondary structure of T4 phage lysozyme. *Biochimica et Biophysica Acta (BBA) - Protein Structure*, *405*(2), 442–451. https://doi.org/10.1016/0005-2795(75)90109-9

Miller, S. D., Straka, W., III, Mills, S. P., Elvidge, C. D., Lee, T. F., Solbrig, J., et al. (2013). Illuminating the capabilities of the suomi national polar-orbiting partnership (NPP) visible infrared imaging radiometer suite (VIIRS) Day/night band. *Remote Sensing*, *5*(12), 6717–6766. https://doi.org/10.3390/rs5126717

Mitchell, E. J., Newell, P. T., Gjerloev, J. W., & Liou, K. (2013). A model of auroral precipitation based on SuperMAG generalized auroral electrojet and substorm onset times. *Journal of Geophysical Research: Space Physics*, *118*(6), 3747–3759. https://doi.org/10.1002/jgra.50343

Mooney, M. K., Marsh, M. S., Forsyth, C., Sharpe, M., Hughes, T., Bingham, S., et al. (2021). Evaluating auroral forecasts against satellite observations. *Space Weather*, *19*(8), e2020SW002688. https://doi.org/10.1029/2020SW002688

Morley, S. K. (2020). Challenges and opportunities in magnetospheric space weather prediction. *Space Weather*, *18*(3), e2018SW002108. https://doi.org/10.1029/2018sw002108

Newell, P. T., Liou, K., Zhang, Y., Sotirelis, T., Paxton, L. J., & Mitchell, E. J. (2014). OVATION Prime-2013: Extension of auroral precipitation model to higher disturbance levels. *Space Weather*, *12*(6), 368–379. https://doi.org/10.1002/2014sw001056

Newell, P. T., Sotirelis, T., Liou, K., Lee, A. R., Wing, S., Green, J., & Redmon, R. (2010). Predictive ability of four auroral precipitation models as evaluated using Polar UVI global images. *Space Weather*, *8*(12), S12004. https://doi.org/10.1029/2010sw000604

Newell, P. T., Sotirelis, T., Liou, K., Meng, C.-I., & Rich, F. J. (2007). A nearly universal solar wind-magnetosphere coupling function inferred from 10 magnetospheric state variables. *Journal of Geophysical Research*, *112*(A1), A01206. https://doi.org/10.1029/2006JA012015

Nishiyama, T., Sakanoi, T., Miyoshi, Y., Katoh, Y., Asamura, K., Okano, S., & Hirahara, M. (2011). The source region and its characteristic of pulsating aurora based on the Reimei observations. *Journal of Geophysical Research*, *116*(A3), A03226. https://doi.org/10.1029/2010ja015507

Obuchi, Y., Sakanoi, T., Yamazaki, A., Ino, T., Okano, S., Kasaba, Y., et al. (2008). Initial observations of auroras by the multi-spectral auroral camera on board the Reimei satellite. *Earth Planets and Space*, *60*(8), 827–835. https://doi.org/10.1186/bf03352834

Papitashvili, N. E., & King, J. H. (2020). OMNIweb. https://doi.org/10.48322/gbpg-5r77

Rao, J., Partamies, N., Amariutei, O., Syrjasuo, M., & van de Sande, K. E. A. (2014). Automatic auroral detection in color all-sky camera images. *IEEE Journal of Selected Topics in Applied Earth Observations and Remote Sensing*, *7*(12), 4717–4725. https://doi.org/10.1109/jstars.2014.2321433

Román, M. O., & Stokes, E. C. (2015). Holidays in lights: Tracking cultural patterns in demand for energy services. *Earth's Future*, *3*(6), 182–205. https://doi.org/10.1002/2014ef000285

Shao, X., Cao, C., Liu, T.-C., Zhang, B., Fung, S. F., & Sharma, A. S. (2016). VIIRS Day/Night Band observations of auroral activity during a 2015 severe geomagnetic storm. *2016 IEEE International Geoscience and Remote Sensing Symposium (IGARSS)* (pp. 3021–3024). IEEE.

Shao, X., Cao, C., Liu, T.-C., Zhang, B., & Wang, W. (2015). Auroral activities observed by SNPP VIIRS day/night band during a long period geomagnetic storm event on April 29–30, 2014. In *SPIE Remote Sensing*.

Syrjasuo, M., & Partamies, N. (2012). Numeric features for detection of aurora. *IEEE Geoscience and Remote Sensing Letters*, *9*(2), 176–179. https://doi.org/10.1109/lgrs.2011.2163616

THEMIS. (n.d.). Retrieved from http://themis.igpp.ucla.edu/

VIIRS Land. (n.d.). Retrieved from https://viirsland.gsfc.nasa.gov/

Wang, Q., Liang, J., Hu, Z.-J., Hu, H.-H., Zhao, H., Hu, H.-Q., et al. (2010). Spatial texture based automatic classification of dayside aurora in all-sky images. *Journal of Atmospheric and Solar-Terrestrial Physics*, *72*(5–6), 498–508. https://doi.org/10.1016/j.jastp.2010.01.011

Yau, A. W., & James, H. G. (2011). Scientific objectives of the Canadian CASSIOPE Enhanced Polar Outflow Probe (e-POP) small satellite mission. In J. S. Almeida & M. P. Miralles (Eds.), *IAGA Special Sopron Book Series* (Vol. 4, pp. 355–364). Springer.

Erratum

In the originally published article, the caption for Figure 2 read as follows: "The Kp index over the 3 days starting March 16 shows the evolution of the geomagnetic storm with red bars indicating high activity. The times shown are CDT at the height of the storm. Credit: NOAA." The caption has been changed to: "The Kp index over the 3 days starting March 16 shows the evolution of the geomagnetic storm with red bars indicating high activity. The times shown are UTC at the height of the storm." This may be considered the authoritative version of record.